Fuel 185 (2016) 370–380

Contents lists available at ScienceDirect

Fuel

journal homepage: www.elsevier.com/locate/fuel

Full Length Article

Aerodynamic breakup of an *n*-decane droplet in a high temperature gas environment

George Strotos [a,b,*], Ilias Malgarinos [a], Nikos Nikolopoulos [a,c], Manolis Gavaises [a]

[a] School of Engineering and Mathematical Sciences, City University London, Northampton Square, EC1V 0HB London, UK
[b] Technological Education Institute of Piraeus, Mechanical Engineering Department, Fluid Mechanics Laboratory, 250 Thivon and P. Ralli str., Aigaleo 12244, Greece
[c] Centre for Research and Technology Hellas/Chemical Process and Energy Resources Institute (CERTH/CPERI), Egialeias 52, Marousi, Greece

ARTICLE INFO

Article history:
Received 7 May 2016
Received in revised form 29 July 2016
Accepted 1 August 2016

Keywords:
Droplet breakup
VOF
Heating
Evaporation

ABSTRACT

The aerodynamic droplet breakup under the influence of heating and evaporation is studied numerically by solving the Navier-Stokes, energy and transport of species conservation equations; the VOF methodology is utilized in order to capture the liquid-air interphase. The conditions examined refer to an *n*-decane droplet with Weber numbers in the range 15–90 and gas phase temperatures in the range 600–1000 K at atmospheric pressure. To assess the effect of heating, the same cases are also examined under isothermal conditions and assuming constant physical properties of the liquid and surrounding air. Under non-isothermal conditions, the surface tension coefficient decreases due to the droplet heat-up and promotes breakup. This is more evident for the cases of lower Weber number and higher gas phase temperature. The present results are also compared against previously published ones for a more volatile *n*-heptane droplet and reveal that fuels with a lower volatility are more prone to breakup. A 0-D model accounting for the temporal variation of the heat/mass transfer numbers is proposed, able to predict with sufficient accuracy the thermal behavior of the deformed droplet.

1. Introduction

The efficiency of spray combustion systems is determined by the dispersion of the spray droplets which increase the surface area and subsequently the rates of heat and mass transfer. Following the primary jet breakup, the produced droplets are subjected to secondary breakup which further enhances the heat/mass transfer rates. The coupled problem of secondary droplet breakup under the influence of heating and evaporation is of major engineering interest, but due to its complexity has not been yet addressed in detail and the vast majority of relevant works examine these two phenomena independently.

Droplets under the influence of aerodynamic forces are subjected to different breakup modes, namely the bag breakup, the transitional breakup, the sheet-thinning breakup and the catastrophic breakup; for details see Guildenbecher et al. [1] among many others. The outcome of the breakup is determined by the relative strength of the aerodynamic, surface tension, viscous and external body forces acting on the droplet. These are grouped into dimensionless numbers, forming the Weber number (We), the Reynolds number (Re), the Ohnesorge number (Oh), the density ratio (ε) and the viscosity ratio (N), as shown in Eq. (1), while under certain flow conditions other parameters such as the Froude number, the Mach number and the turbulence levels may become important.

$$We = \frac{\rho_g U_{rel,0}^2 D_0}{\sigma} \quad Re = \frac{\rho_g U_{rel,0} D_0}{\mu_g} \quad Oh = \frac{\mu_l}{\sqrt{\rho_l \sigma D_0}}$$
$$\varepsilon = \frac{\rho_l}{\rho_g} \quad N = \frac{\mu_l}{\mu_g} \tag{1}$$

The phenomena observed during droplet breakup have been addressed in review studies such as those of [1–5] among others; it is generally considered that the We number is the most influential parameter, while viscous effects become important when $Oh > 0.1$. The breakup process requires some finite time to be established and the duration of the phenomenon is in the order of the shear breakup timescale t_{sh} proposed by Nicholls and Ranger [6]:

$$t_{sh} = \frac{D_0}{U_{rel,0}} \sqrt{\varepsilon} \tag{2}$$

* Corresponding author at: School of Engineering and Mathematical Sciences, City University London, Northampton Square, EC1V 0HB London, UK.
E-mail addresses: George.Strotos.1@city.ac.uk, gstrot@teipir.gr (G. Strotos), Ilias.Malgarinos.1@city.ac.uk (I. Malgarinos), Nikolaos.Nikolopoulos.1@city.ac.uk, n.nikolopoulos@certh.gr (N. Nikolopoulos), M.Gavaises@city.ac.uk (M. Gavaises).

http://dx.doi.org/10.1016/j.fuel.2016.08.014
0016-2361/

Nomenclature

Roman symbols

B_M	mass transfer Spalding number [–]
B_T	heat transfer Spalding number [–]
c_p	heat capacity [J/kg K]
D	diameter [m]
D_{AB}	vapor diffusion coefficient [m^2/s]
F_{heat}	heating factor [–]
Oh	Ohnesorge number $Oh = \mu_l/\sqrt{\rho_l \sigma D_0}$ [–]
k	thermal conductivity [W/mK]
L	latent heat of vaporization [J/kg]
m	mass [kg]
$\dot{m}''$	evaporation rate per unit area [kg/m^2 s]
Nu	Nusselt number [–]
Pr	Prandtl number [–]
R	radius [m]
Re	Reynolds number $Re = \rho_g U_{rel,0} D_0/\mu_g$ [–]
S	surface area [m^2]
Sc	Schmidt number [–]
Sh	Sherwood number [–]
t	time [s]
t_{sh}	shear breakup timescale $t_{sh} = D\sqrt{\varepsilon}/U$ [–]
T	temperature [K]
U	reference velocity [m/s]
u	instantaneous droplet velocity [m/s]
V	volume [m^3]
We	Weber number $We = \rho_g U_{rel,0}^2 D_0/\sigma$ [–]
We_t	instantaneous We number [–]
Y	vapor concentration [kg/kg]

Greek symbols

a	thermal diffusivity [m^2/s]
γ	thermal effusivity $\gamma = \sqrt{k\rho c_p}$ [J/m^2 K $s^{0.5}$]
ε	density ratio $\varepsilon = \rho_l/\rho_g$ [–]
μ	viscosity [kg/ms]
N	viscosity ratio $N = \mu_l/\mu_g$ [–]
ν	kinematic viscosity [m^2/s]
ρ	density [kg/m^3]
σ	surface tension coefficient [N/m]

Subscripts

0	initial
c	cross-stream
cr	critical
g	gas
l	liquid
rel	relative
s	at surface
t	instantaneous magnitude
x, y, z	coordinates
∞	free-stream conditions

Abbreviations

C07	*n*-heptane C_7H_{16}
C10	*n*-decane $C_{10}H_{22}$
CFD	Computational Fluid Dynamics
cpR	Cells per Radius
CSS	Continuum Surface Stress
UDF	User Defined Function
VOF	Volume of Fluid

Many works have studied either experimentally or numerically the droplet breakup, aiming to enlighten the conditions leading to the different breakup regimes and the underlying physics. Selective experimental studies on droplet breakup are those of [7–22] but generally, there is a scattering of the experimental findings which is probably due to the variety of the experimental techniques used and the experimental uncertainties. Numerical works aiming to fill the gap in knowledge such as those of [23–32]; they have examined the isothermal droplet breakup in 2-D and 3-D computational domains and they have provided useful information into the detailed processes inside and in the vicinity of the droplets during droplet breakup, which are difficult to be determined with experimental techniques. More specifically, [7–10] provided breakup maps in the *We-Oh* plane, [11–13,16] further clarified the boundaries between different breakup regimes, [14,15,20,23,25,30,31] clarified the physical mechanisms behind the breakup regimes, [13,18] examined the size distribution of the child droplets after the parent droplet disintegration, [22] identified experimentally the gas flow structure during droplet breakup, [15,24,26,32] examined the effect of density ratio and [26,27,29,31] examined the droplet drag coefficient. For a detailed presentation of the works referring to droplet breakup, see Strotos et al. [33].

Regarding the evaporation studies, in addition to 0-D or 1-D models (see details in the review articles of [34–37] among others), detailed CFD works solving the complete Navier-Stokes and heat/mass transfer equations have also been published. Selectively, the works of [38–47] refer to single component evaporation and [48–53] refer to multicomponent droplet evaporation, providing detailed information in the transport processes between the liquid and the gas phase. More specifically, [39,40] were the first who solved the complete set of the governing equations, [42,47] modelled the presence of the suspender, [43] examined the effect of thermocapillary flow, [44] studied the effect of turbulence and [46] proposed numerical improvements for the evaporation modelling. Similarly, in multicomponent studies the first ones were those of [48,49], followed by [50] who included variable thermophysical properties and [52,53] which conducted parametric studies. The aforementioned studies were restricted to the modelling of isolated spherical droplets and a detailed presentation of the works referring to droplet evaporation, was given in Strotos et al. [54].

Regarding the coupled problem of droplet breakup and evaporation, this has not yet been studied in detail except in the CFD works of [55–60]. Haywood et al. [55,56] showed that for droplets under steady or unsteady (oscillatory) deformation, the quasi-steady correlations for Nusselt (*Nu*) and Sherwood (*Sh*) numbers are still valid when a volume-equivalent diameter is used, Mao et al. [57] showed that the mass transfer from deformed droplets is mainly controlled by the Peclet (*Pe*) number, while the *We* number has a small impact only at high *Pe* numbers. Hase and Weigand [58] studied the effect of droplet deformation on the heat transfer enhancement and they found that this increases due to the oscillatory droplet motion and the increased surface area of the deformed droplets; moreover, the steady-state classical correlations for the *Nu* number, under-predict the heat transfer at the beginning of the simulation. Later, Schlottke et al. [59] included the evaporation in their model and they found that the droplet heating is affected by the flow field inside the droplet which transfers hotter fluid from the droplet surface towards inside. Cerqueira et al. [60] studied spherical and deformed rising bubbles and proposed new correlations for the *Nu* and *Sh* numbers.

The aforementioned studies were restricted to *We* number below 10, which limits the results to small droplet deformation without breakup. Recently, Strotos et al. [61] examined the effect of heating and evaporation in cases undergoing breakup for *We* = 15–90. They examined volatile *n*-heptane droplets and they showed that the droplet heating becomes increasingly influential during breakup for lower *We* number and higher gas temperature. The present numerical work is a continuation of this work and examines an *n*-decane droplet with substantially lower volatility than the *n*-heptane; this promotes the higher heating of the droplet. This work is the first examining the combined effect of heating and breakup solving the Navier-Stokes, energy and transport of species equations coupled with interface capturing, for a wide range of We numbers, gas phase temperatures for this particular fuel while it compares it with the less volatile one for similar flow conditions. The structure of the paper includes a brief description of the numerical model and the cases examined, followed by the results, while the most important conclusions are summarized at the end.

2. Numerical model and methodology

The continuous field representation of the two-phase flow with the VOF methodology is used to study the droplet breakup. The problem is assumed to be 2-D axisymmetric and an automatic local grid refinement technique [62,63] enhances the accuracy of the computations at the interface region, while achieving low computational cost compared to a simulation with a uniform grid of the same density. The droplet heating and evaporation are accounted for by solving the energy and vapor transport equations, while the local evaporation rate is obtained by using a model based on Fick's law, which is independent of the droplet shape. The species properties depend on the local temperature [64,65] and mass averaging rules are used for the gaseous mixture assuming incompressible ideal gas. For the complete presentation of the equations solved, the reader is referred to Strotos et al. [54]. The simulations were performed with the commercial CFD tool ANSYS FLUENT v14.5 [66] and the numerical settings adopted as also the User Defined Functions (UDFs) are identical to those used in Strotos et al. [61].

The model has been successfully validated in [33,54,63,67,68] for cases including the motion of a free falling droplet, droplet breakup, droplet evaporation and droplet impact onto a solid substrate.

3. Results and discussion

3.1. Cases examined and numerical setup

The cases examined are similar to those presented in Strotos et al. [61] for a volatile *n*-heptane droplet (C07), but this time an *n*-decane (C10) droplet is examined which has a much lower volatility (i.e. vapor pressure) than the *n*-heptane. The cases examined refer to a small 100 μm diameter droplet with an initial temperature of T_0 = 300 K, corresponding to *Oh* = 0.02 which is low enough to guarantee breakup process almost independent from the *Oh* number. The droplet is assumed to be initially motionless and it is subjected to a step change of the gas phase velocity leading to *We* numbers in the range 15–90. The ambient air has a high temperature in the range 600–1000 K ($T_{cr,C10}$ = 617.7 K) which correspond to high density and viscosity ratios ($\varepsilon > 1200$ and $N > 20$ respectively) and thus the breakup outcome is not affected by them since $\varepsilon > 32$ [24]. The aforementioned combination of *We* numbers and gas phase temperatures corresponds to gas phase velocities in the range 77–243 m/s; these in turn correspond to *Re* numbers in the range 84–367 which ensures that the flow remains laminar and axisymmetric [69,70]; the Mach numbers are below 0.38, which implies that the compressibility effects can be ignored. For all cases examined, the ambient pressure is atmospheric; thus no modifications capturing high pressure effects are required in the evaporation model. A graphical representation of the cases examined is shown in Fig. 1 on the *We*-*Re* map. These cases were examined both for evaporating and isothermal conditions. For the latter, the energy equation and the evaporation source terms were not accounted for, while the species properties were kept constant at their reference temperature values, i.e. at T_0 = 300 K for the liquid droplet and at T_∞ for the surrounding air; the isothermal runs correspond to a parametric study for the effect of *We* and *Re* numbers.

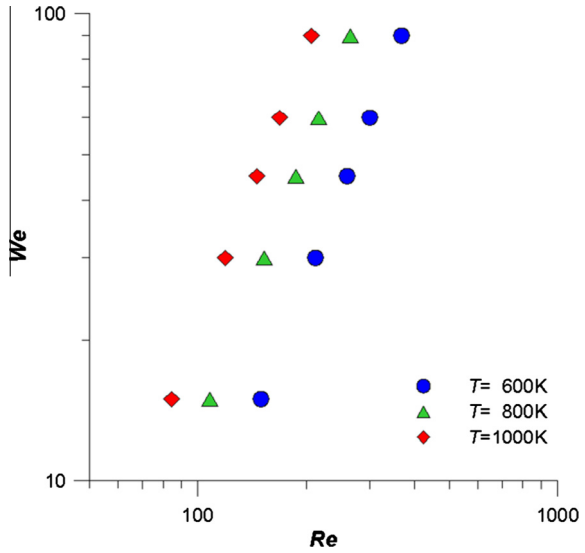

Fig. 1. Cases examined on the *We*-*Re* plane.

Regarding the computational domain and the boundary conditions, these are the same as in Strotos et al. [33,61,68], in which a step change of the gas phase velocity is applied around the initially motionless droplet; the 2-D axisymmetric computational domain is moving with the average translational droplet velocity. Upwind the droplet, Dirichlet boundary conditions were applied (i.e. fixed velocity and temperature for the non-isothermal cases) and downwind Neumann boundary conditions (i.e. zero first gradient for all variables) were used. A locally refined grid with 192 cells per radius was used, able to resolve the boundary layers at the interface region as explained in Strotos et al. [61]. It has to be noted that the 2D simulations performed in this work are considered reliable up to the breakup instant, since after that, three-dimensional phenomena appear.

In an effort to relate and also distinguish the simulations performed in Strotos et al. [61] for the volatile *n*-heptane droplet, from the present simulations referring to *n*-decane, the heat and mass transfer Spalding numbers (B_T and B_M respectively) are considered (Eqs. (3) and (4)). These are calculated by using the initial surface temperature $T_{s,0}$ (Eq. (5)) which corresponds to the contact temperature between semi-infinite solids [71]; this concept was also used in [72–74] for droplet impact on hot substrates and agrees well with the CFD predictions at the first time-step.

$$B_{T,\infty} = \frac{c_{p,g,\infty}(T_\infty - T_0)}{L(T_{s,0})} \tag{3}$$

$$B_{M,0} = \frac{Y_s(T_{s,0}) - Y_\infty}{1 - Y_s(T_{s,0})} \tag{4}$$

$$T_{s,0} = \frac{\gamma_l T_0 + \gamma_g T_\infty}{\gamma_l + \gamma_g} \tag{5}$$

$$F_{heat} = \frac{1 + B_{T,\infty}}{1 + B_{M,0}} \tag{6}$$

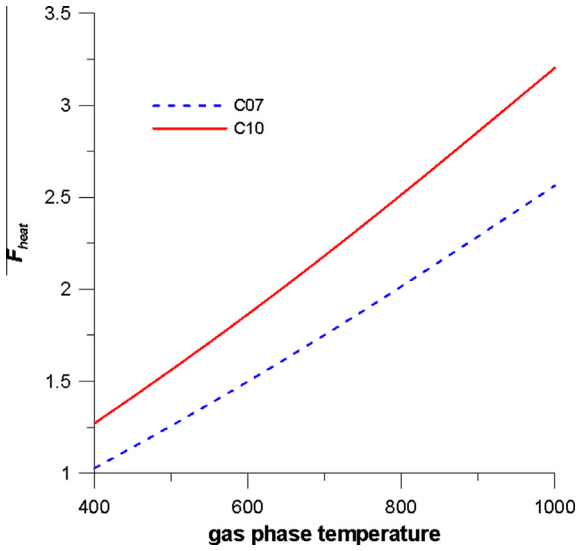

Fig. 2. Heating factor as a function of the gas phase temperature for two different fuels (T_0 = 300 K).

The droplet's tendency to increase its temperature is proportional to B_T and inversely proportional to B_M, since the evaporation absorbs heat and tends to decrease the droplet temperature. An indicator of the droplet heat-up is the heating factor F_{heat} (Eq. (6)); large values imply a high tendency to increase the temperature. A comparison of the heating factor for the *n*-heptane (C07) and the *n*-decane (C10) is shown in Fig. 2 as a function of the gas phase temperature for T_0 = 300 K (note that this is independent of the flow conditions). It is evident that the *n*-decane has a higher possibility to heat-up due to its lower vapor pressure; the heating factor increases with the gas phase temperature and decreases with increasing initial fuel temperature (not shown in Fig. 2). It has to be noted that the heating factor has a qualitative character and for the isothermal cases it was assumed that F_{heat} = 1, which corresponds to infinite latent heat and zero vapor pressure. Note that the definition of the heating factor adopted here is suitable for the present conditions, but might not be suitable for low ambient temperatures close to the droplet temperature in which F_{heat} < 1.

Finally, prior to the presentation of the results of the present work, it has to be noted that the isothermal simulations conducted in Strotos et al. [61] for an *n*-heptane and the present simulations for an *n*-decane are in close agreement between them since they both have low *Oh* numbers (0.01 and 0.02 respectively) and similar *Re* number ranges (77–337 and 84–367 respectively for T_∞ = 600–1000 K). On the other hand, the evaporating simulations for these two fuels are exhibiting large variations due to the species thermal properties.

3.2. Hydrodynamic effect of heating

The results obtained for the droplet shapes are shown in Figs. 3 and 4 for the cases with free stream temperature 800 and 1000 K respectively. In these figures the left part corresponds to the isothermal predictions and the right part to the evaporating simulations; the cases with T_∞ = 600 K are not presented since the differences between isothermal and evaporating simulations were small. The droplet shapes drawn in black correspond to time intervals of $0.5t_{sh}$ (i.e. 0.0, 0.5, 1.0, 1.5, $2.0t_{sh}$) and the droplet shapes drawn in red correspond to intermediate instances i.e. 0.75, 1.25, 1.75, $2.25t_{sh}$ (the time instant of $0.25t_{sh}$ has been omitted); the last droplet shape corresponds to the instant of breakup. From figures Figs. 3 and 4 it is evident that the *We* number is the most influential parameter leading to different breakup regimes as the *We* number increases, namely the bag breakup for low *We* numbers, the transitional breakup for intermediate *We* numbers and the sheet-thinning breakup for the highest *We* number examined. Nevertheless, the sheet-thinning breakup is not clear due to the low *Re* number and the continuous transition between the different breakup regimes; the effect of *Re* number and the existence of a critical *Re* number leading to bag breakup at *We* = 15 was in detail discussed in Strotos et al. [61] and similar comments were also made in Han and Tryggvason [23] and Guildenbecher et al. [1].

Apart from the dominant role of *We* number, the droplet heating is playing an important role for the low *We* number cases. Under isothermal conditions, droplets with *We* = 15 and T_∞ > 800 K are not breaking up due to the low *Re* number. At the same *We* number when heating is accounted for with T_∞ = 800 K (Fig. 3), a clear bag breakup is predicted; this is even more emphatic for the case of T_∞ = 1000 K (Fig. 4) in which the droplet not only breaks up, but the breakup regime predicted is the transitional breakup. To the authors best knowledge, no previous study has reported transitional break-up at such a low *We* number; this is purely due to the droplet heating which reduces the surface tension coefficient and subsequently the forces tending to resist the droplet deformation. Note that the effect of heating was not so profound in the high volatility *n*-heptane examined in Strotos et al. [61].

The predicted onset of breakup t_{br} (termed also as "initiation time") for all cases examined is shown in Fig. 5, along with the corresponding experimental correlations given by Pilch and Erdman [2] and Dai and Faeth [13], abbreviated as "P-E 1987" and "D-F 2001" respectively; the present data for the breakup time are subjected to error of the order of $0.05t_{sh}$ (2.5–5%) due to the estimation of the breakup time by examining post-processed images. The experimental correlations differ between them due to several experimental uncertainties [25]. The trends are correctly captured by predicting faster breakup with increasing *We* number. The isothermal cases exhibit a weak dependency on *Re* number when the *We* is kept constant, while in the evaporating cases the reduction of the surface tension coefficient acts as if the *We* number was higher; subsequently the droplet breaks up is faster. A best fit curve of the breakup time for both evaporating and isothermal cases is given in Eq. (7) valid for the entire range of conditions examined, i.e. *n*-decane fuel, *Oh* = 0.02, *We* = 15–90, *Re* = 84–367 and T_∞ = 600–1000 K.

$$t_{br}/t_{sh} = 8.628We^{-0.352}Re^{-0.086}F_{heat}^{-0.116} \quad (7)$$

One of the most important magnitudes determining the combustion efficiency is the droplet surface area (*S*) which deviates significantly from the corresponding of the initial spherical shape (S_0) during the droplet deformation and breakup and it is difficult to be measured experimentally. The temporal evolution of this quantity is presented in Fig. 6 for selected cases (T_∞ = 800 K and *We* = 15, 30, 90); note that for the isothermal case with *We* = 15, the droplet is not breaking up. In all cases, after an initial non-deforming period of $\sim 0.3t_{sh}$, the droplet surface area starts to increase with a fast rate (1.6–5.7 in terms of non-dimensional units) proportional to the *We* number, which is in accordance with the findings of Han and Tryggvason [23]. Up to $t = t_{sh}$ the variation of the surface area is smooth, but at subsequent times the rate of deformation may change due to surface instabilities appearing even in the isothermal cases. For that reason, the maximum surface area at the instant of breakup is not following a smooth variation as the *We* number is changing and a local maximum is observed at *We* = 30 (as it was also shown in [61]) reaching values of $12S_0$. This point needs further investigation by performing 3-D simulations since 3-D phenomena may appear before the breakup instant and alter both the rate of deformation

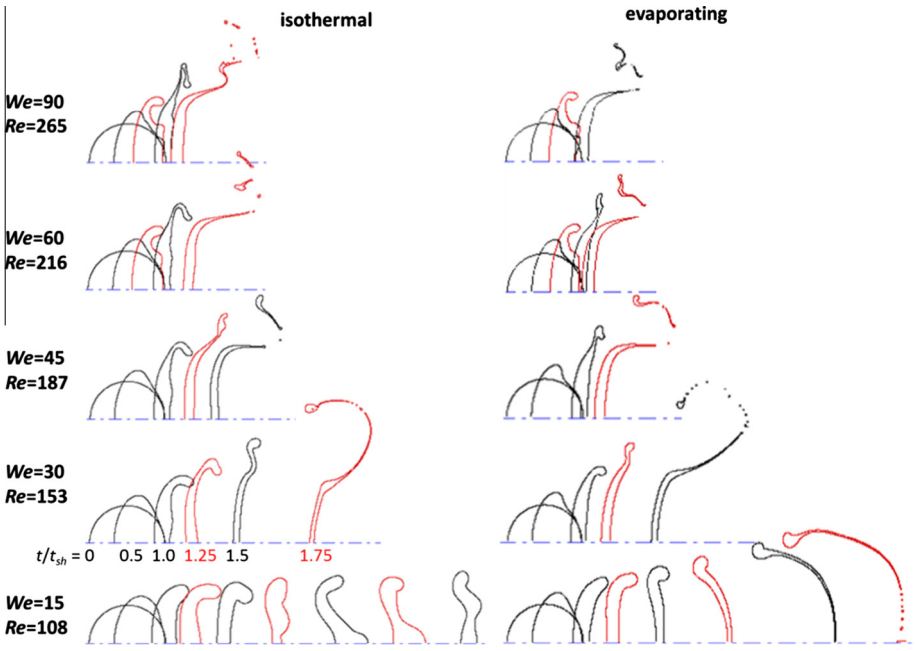

Fig. 3. Droplet shape evolution for the cases with T_∞ = 800 K. The droplet shapes drawn black (see the online version) correspond to time intervals of $0.5t_{sh}$ and the droplet shapes drawn red correspond to representative intermediate instances of $0.25t_{sh}$. The last droplet shape corresponds to the instant of breakup. Differences are observed at the lower *We* number case. (For interpretation of the references to colour in this figure legend, the reader is referred to the web version of this article.)

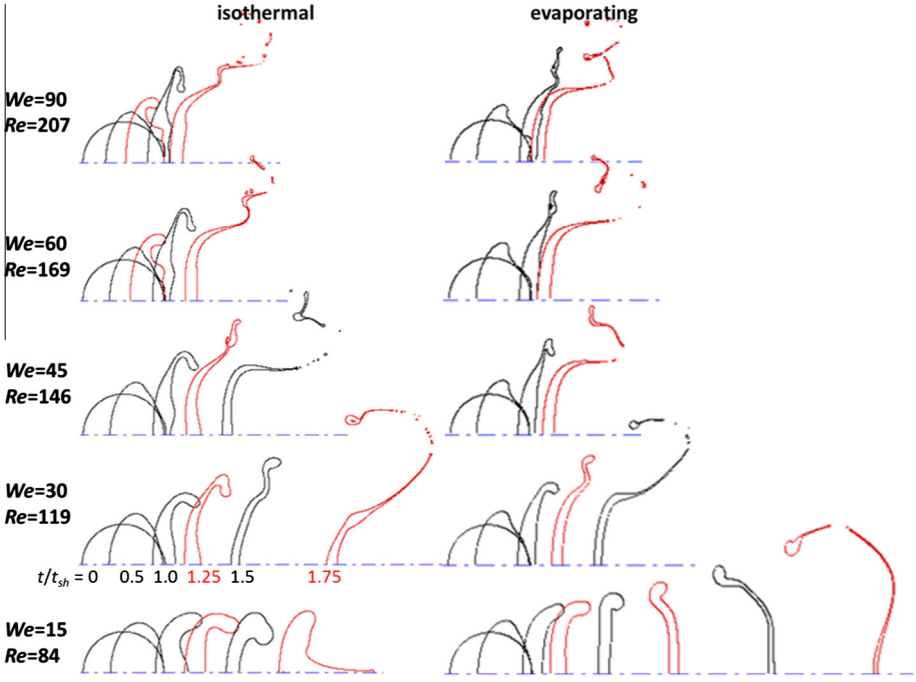

Fig. 4. Droplet shapes for the cases with T_∞ = 1000 K. The droplet shapes drawn black (see the online version) correspond to time intervals of $0.5t_{sh}$ and the drawn red correspond to representative intermediate instances of $0.25t_{sh}$. The last droplet shape corresponds to the instant of breakup. Differences are observed at the lower *We* number case. (For interpretation of the references to colour in this figure legend, the reader is referred to the web version of this article.)

as also the breakup instant. Regarding the effect of heating (see the solid lines in Fig. 6), it is evident that it is important for low to medium *We* numbers and $t > t_{sh}$ by further increasing the rate of deformation.

As explained in Strotos et al. [61] it is difficult to find a mathematical expression predicting the temporal evolution of the surface area for the entire phenomenon up to the breakup instant and covering the entire range of *We* numbers leading to different breakup regimes. This becomes even more complex when heating is included since the surface area evolution is implicitly coupled with the variation of the surface tension coefficient due to heating. On the other hand, the evolution of the surface area can be predicted for $t < t_{sh}$ with Eq. (8a), which has been slightly modified relative to the one used in [61] by using in the denominator on the right hand side of Eq. (8a) the term $\sin h(c_2)$. Now, the coefficient c_1 expresses the surface area at $t = t_{sh}$ and c_2 characterizes the form of the curve connecting the initial and the "final" state at $t = 0$ and $t = t_{sh}$ respectively; a low c_2 value implies a smoother (closer to the linear)

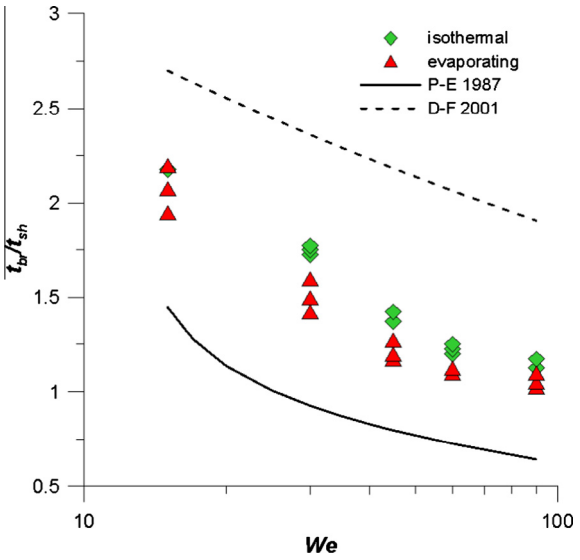

Fig. 5. Predicted dimensionless breakup time for the isothermal and the evaporating *n*-decane cases.

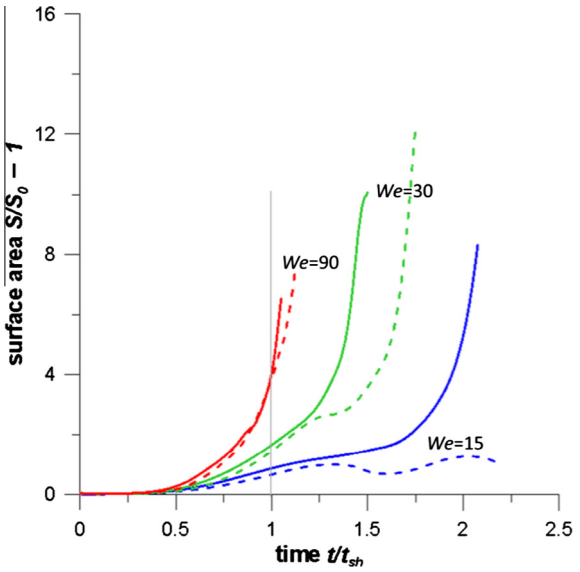

Fig. 6. Temporal evolution of the dimensionless droplet surface area for selected cases with T_∞ = 800 K. The dashed lines correspond to the isothermal cases and the solid lines to the evaporating cases.

variation. An important improvement of the present fitting curve relative to the one in [61], is the inclusion of the effect of heating by using the correction factor f_{corr} in the adjustable coefficients c_1 and c_2 (see Eqs. (8b) and (8c)). Eqs. (8a)–(8c) is valid for the entire range of conditions examined in the present work, the correlation coefficient for the fitting of the surface area evolution is above 0.98 and the prediction of the surface area at $t = t_{sh}$ is within the 15% error for most of the cases examined; nevertheless this can reach values of 30% for specific cases at the highest temperature of 1000 K.

$$\frac{S}{S_0} - 1 = c_1 \frac{\sin h(c_2 \cdot t/t_{sh})}{\sin h(c_2)}, \quad t < t_{sh} \tag{8a}$$

$$c_1 = 0.1484 We^{1.092} Re^{-0.284} f_{corr}, \quad f_{corr} = 1 + 4.152 We^{-1.06} (F_{heat} - 1)^{0.84} \tag{8b}$$

$$c_2 = 4.5234 We^{0.294} Re^{-0.198} f_{corr}, \quad f_{corr} = 1 - 0.013 We^{-0.50} (F_{heat} - 1)^{0.289} \tag{8c}$$

For the isothermal cases (f_{corr} = 1) the surface area increases with increasing *We* number and decreasing *Re* number; this is clearly derived from the sign of the exponents of c_1 (Eq. (8b)). When heating is included, the phenomenon becomes more complicated and the correction factor f_{corr} depends both on the *We* number and the heating factor F_{heat}. The correction factor for the coefficient c_1 is always $f_{corr} > 1$ which means that heating tends to increase the surface area at $t = t_{sh}$. As stated in [61], the extrapolation of this curve up to t_{br} should be done with caution and limit the maximum value not to exceed $10–12S_0$, otherwise unphysical values may be obtained.

The droplet breakup is governed by the relative strength of the forces acting on the droplet, which vary dynamically as the droplet shape, dimensions and velocity change during the whole process. The instantaneous deforming forces scale with $\rho_g u_{rel,t}^2 D_{c,t}^2$ where $u_{rel,t}$ is the instantaneous relative drop-gas velocity (obtained by subtracting the average droplet velocity from the free-stream velocity) and $D_{c,t}$ is the instantaneous cross-stream diameter, while the instantaneous restorative forces scale with $\sigma D_{c,t}$ in which the viscous forces have been ignored since *Oh* < 0.1. The ratio of these forces represents an instantaneous *We* number (see Eq. (9)) which changes during the breakup process and includes the effects of heating, deformation and velocity change:

$$We_t = \frac{\rho_g u_{rel,t}^2 D_{c,t}}{\sigma} = We_0 \left(\frac{\sigma_0}{\sigma}\right) \left(\frac{D_{c,t}}{D_0}\right) \left(\frac{u_{rel,t}}{U_0}\right)^2 \tag{9}$$

The predicted transient *We* number based on Eq. (9) is plotted in Fig. 7 for selected isothermal and evaporating cases with T_∞ = 800 K. The transient *We* number increases in time implying that the deforming forces become progressively stronger, except of the isothermal case with *We* = 15. In this case the droplet is not breaking up and after reaching a maximum, the instantaneous *We* number decreases, implying that the restorative forces become stronger. Generally, the instantaneous *We* number (as defined in Eq. (9)) increases by a factor of 2–3 relative to the initial *We* number which is mainly ought to the increase of the cross sectional diameter; the reduction of the relative drop-gas velocity (no more than 10% for the cases examined) and the reduction of the surface tension coefficient play a secondary role. In Fig. 7 the curves derived from Eq. (9) by using either the experimental breakup time of Dai and Faeth [13] or that of Pilch and Erdman [2] for *Oh* = 0.02

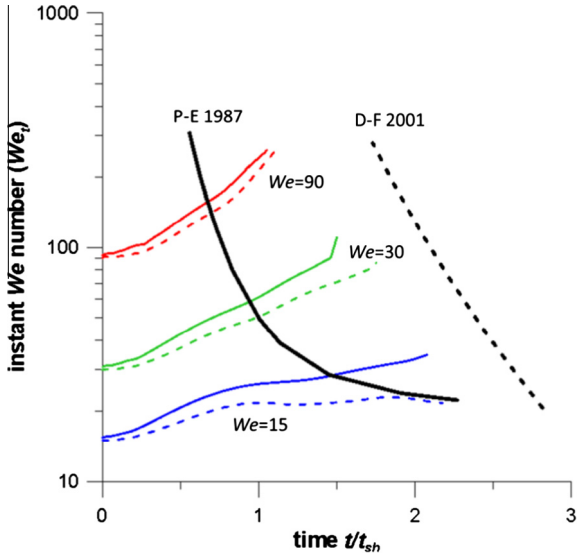

Fig. 7. Predicted instant *We* number for selected isothermal (dashed lines) and evaporating (solid lines) cases with T_∞ = 800 K.

are also shown; these were derived by processing the experimental data of [13] and more details can be found in [61]. These curves represent the critical instantaneous condition for breakup and when crossed, breakup occurs. The present simulations qualitatively agree with these curves.

3.3. Thermal behavior of the droplet

The temporal evolution of the mean volume averaged droplet temperature T_m and the spatially averaged surface temperature T_s are shown in Fig. 8a with the solid and dashed lines respectively, for two cases combining different *We* numbers and gas phase temperatures; these are indicated inside the parentheses as (*We*, T_∞). Both the mean droplet temperature and the surface temperature increase with increasing ambient temperature, as expected. The mean droplet temperature T_m increases continuously in time and may reach a heat-up of 15 K by the onset of breakup, while the average surface temperature T_s exhibits a quite transient behavior; during the flattening phase ($t < 0.6–0.8t_{sh}$) the surface temperature increases until reaching a maximum, followed by a decrease until coming closer to the volume averaged temperature. This behavior is mainly attributed to the flow patterns induced by the shape distortion which exchange hotter fluid from the droplet surface with the colder fluid from the droplet interior (see also Schlottke et al. [59]). Additional to that, the increased surface temperature results in a high evaporation rate which tends to further suppress the surface heating.

In Fig. 8b the dimensionless droplet mass and droplet volume (solid and dashed lines, respectively) are shown for the cases (*We*, T_∞) = (15, 600) and (15, 1000). Up to the breakup instant, the evaporated mass is less than 0.5%, while the droplet volume increases up to 0.1% due to the thermal expansion effect. Note that in the corresponding cases with *n*-heptane presented in [61], the maximum heat-up was 7 K, the evaporated mass was reaching 2% and the thermal expansion effect was absent. The aforementioned differences are mainly affected by the different volatility between the *n*-heptane and *n*-decane.

The heat and mass transfer processes are usually characterized by the dimensionless Nusselt (*Nu*) and Sherwood (*Sh*) numbers respectively, which express the heat/mass transfer enhancement relative to a purely diffusive process. These are defined as the dimensionless temperature/concentration gradient at the droplet interface, but their calculation is not applicable with the VOF

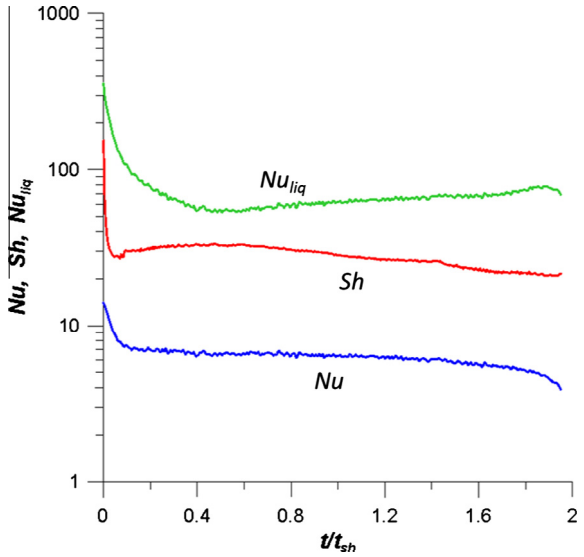

Fig. 9. Temporal variation of *Nu*, *Sh* and Nu_l for the case of (*We*, T_∞) = (15, 600).

methodology due to the continuous variation of the field magnitudes across the interface as explained in [60]. Inspired by Hase and Weigand [58] an indirect method is used to estimate them, through Eqs. (10)–(12):

$$\rho_l V \frac{d(c_{p,l} T_m)}{dt} = S\left(\frac{Nu \cdot k_{g,\infty}}{D_0}(T_\infty - T_s) - \dot{m}'' L\right) \tag{10}$$

$$\dot{m} = S\frac{Sh \cdot \rho_{g,\infty} D_{AB,\infty}}{D_0} ln(1 + B_M) \tag{11}$$

$$Nu_l \cdot k_{l,0}\frac{T_s - T_m}{D_0} = Nu \cdot k_{g,\infty}\frac{T_\infty - T_s}{D_0} - \dot{m}'' L \tag{12}$$

Eq. (10) is the droplet energy balance, Eq. (11) is a widely used relationship for the evaporation rate of spherical droplets and Eq. (12) represents the heat flux continuity at the droplet's surface, in which Nu_l is the dimensionless temperature gradient inside the liquid; this equation connects the average droplet temperature T_m with the surface temperature T_s. The set of Eqs. (10)–(12) also forms a variant of the 0-D model for spherical droplet evaporation proposed by Renksizbulut et al. [75]. Solving Eqs. (10)–(12) for *Nu*, *Sh* and Nu_{liq} and

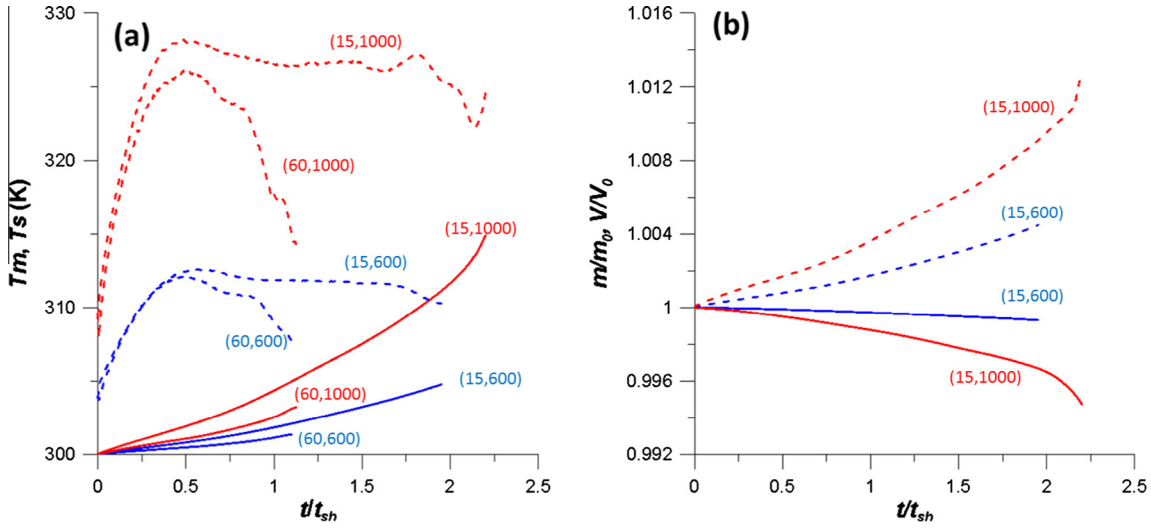

Fig. 8. (a) Temporal evolution of mean droplet temperature T_m (solid lines) and spatially averaged surface temperature T_s (dashed lines). In (b) temporal evolution of dimensionless droplet mass (solid lines) and dimensionless droplet volume (dashed lines). The cases shown in parentheses correspond to (*We*, T_∞).

Table 1
Transient Nu and Nu_{liq} numbers. The time t corresponds to the dimensionless time t/t_{sh}.

	$Nu = c_0 - c_1 t + c_2 \exp(-c_3 t)$	$Nu_l = c_0 + c_1 \exp(-c_2 t) + c_3 \cos(2\pi t/c_4)$
c_0	$1.326 Re_\infty^{0.3647}(1+B_{T,\infty})^{-0.236}$	$56.47 + 7.65\cdot 10^{-4} Re_l^{1.707}(1+B_{T,\infty})^{-0.432}$
c_1	$3\cdot 10^{-6} Re_\infty^{2.212}(1+B_{T,\infty})^{2.226}$	$201 + 1.99\cdot 10^{-4} Re_l^{2.25}(1+B_{T,\infty})^{-0.5285}$
c_2	3	$15.59 + 1.65\cdot 10^{-6} Re_l^{2.64}(1+B_{T,\infty})^{-0.623}$
c_3	60	$5.786\cdot 10^{-5} Re_l^{2.226}(1+B_{T,\infty})^{-0.825}$
c_4	–	1.2

using the CFD data for the mean droplet temperature T_m, the space averaged surface temperature T_s and the evaporation rate dm/dt, the temporal variation of the dimensionless transfer numbers is obtained; this is shown in Fig. 9 for the case $(We, T_\infty) = (15, 600)$, which can be regarded as representative, since the qualitative behavior observed is similar in all cases examined. For the Nu and Sh numbers, there is a short initial transitional period as the one observed in [39,40,58]; after that, they exhibit small fluctuations in time. The Sh number seems to oscillate around a steady-state

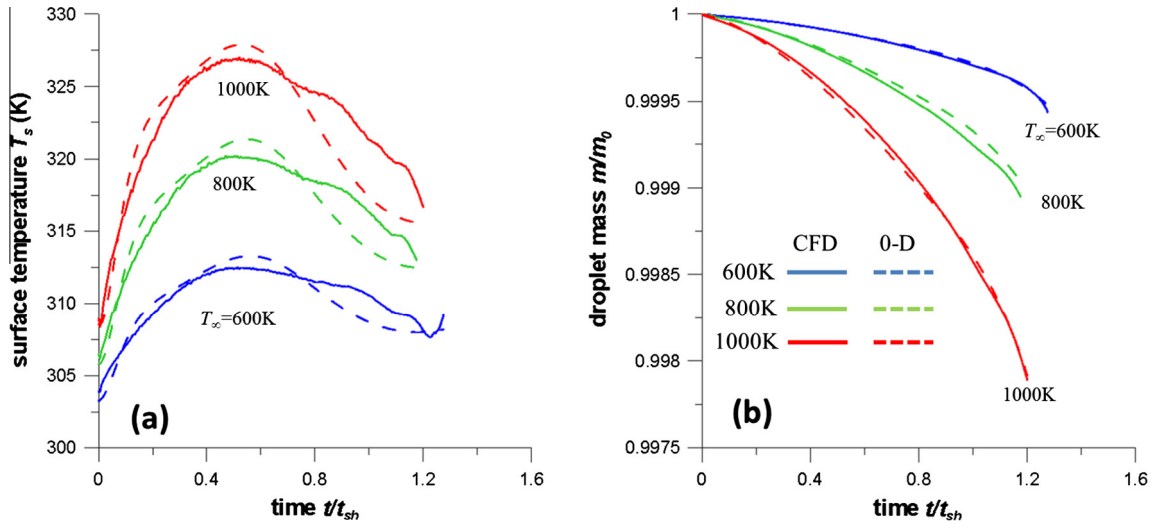

Fig. 10. Predictions of the 0-D model for (a) the spatially averaged surface temperature and (b) the droplet mass for the case of We = 45. The solid lines are the CFD data and the dashed lines are the 0-D model predictions.

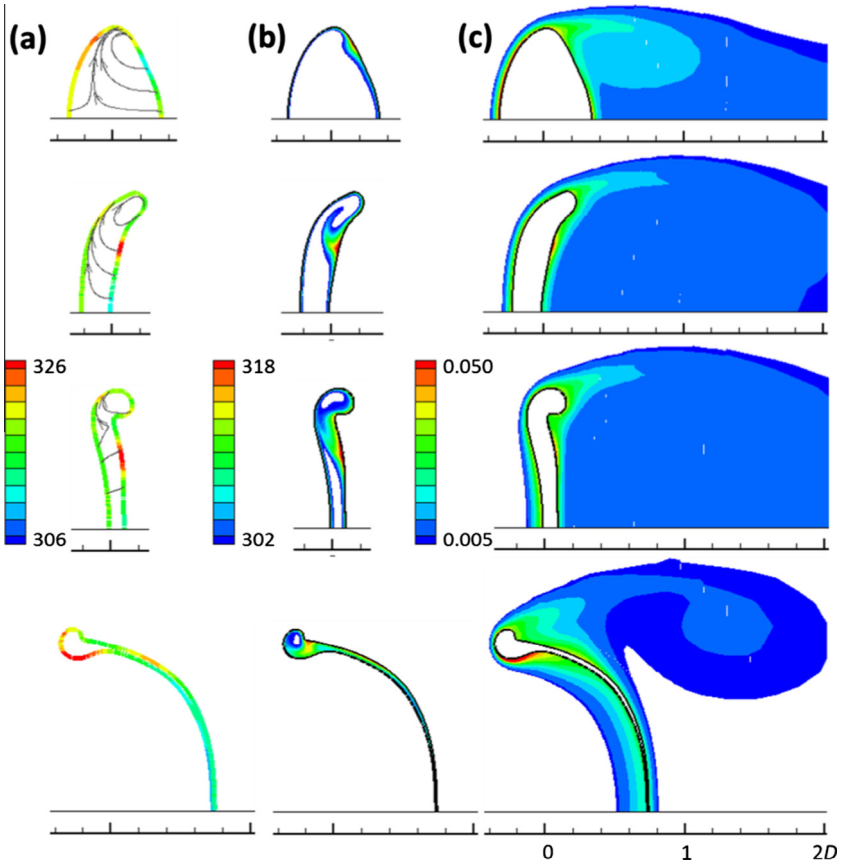

Fig. 11. Spatial distribution of (a) surface temperature, (b) droplet temperature and (c) vapor concentration for the case $(We, T_\infty) = (15, 800)$. The time instances presented are 0.5, 1.0, 1.5 and $2.0 t_{sh}$. In (a) characteristic streamlines are also shown. For color interpretation, see the online version.

value, while the Nu number decreases continuously in time with a slow rate. On the other hand, the Nu_{liq} number exhibits a more unsteady behavior. The initial transitional period is longer compared to the other numbers and its magnitude exhibits almost one order of magnitude larger variations with time.

It is of engineering interest to find expressions for the Nu, Sh and Nu_{liq} numbers and use them in 0-D or 1-D models aiming to predict the droplet temperature and the evaporation rate. Earlier CFD works on spherical droplets (see [39,40] among many others) provided such expressions as a function of the instantaneous Re, B_T and B_M numbers. Nevertheless, this is not applicable in the case of droplet breakup due to the short duration of the phenomenon and more importantly due to shape distortion from the spherical one. In [61] time-averaged transfer numbers (being a function of the initial reference conditions) were used and they could adequately capture the thermal behavior of droplets undergoing breakup. Following this approach, the time-averaged transfer numbers fitting the present data are given in Eqs. (13)–(15); the Re_l appearing in Eq. (15) ($Re_l = Re_\infty \varepsilon^{2/3} N^{-4/3}$) was taken from [38] and it is derived by equating the tangential shear stresses at the droplet surface:

$$\overline{Nu} = \frac{2 + 6.83 Re_\infty^{0.07} Pr_{g,\infty}^{1/3}}{(1 + B_{T,\infty})^{0.75}} \tag{13}$$

$$\overline{Sh} = \left(2 + 1.608 We_0^{0.591} Sc_{g,\infty}^{1/3}\right)(1 + B_{T,\infty}) \tag{14}$$

$$\overline{Nu_l} = 55.95 + Re_l Pr_l^{1.6}/1429 \tag{15}$$

The set of Eqs. (10)–(15) forms a 0-D model which can be used to predict the average droplet heating and evaporation, but not the transient variation of the surface temperature, which decreases after reaching a maximum (see Fig. 8a). The reason for that discrepancy is that the time-averaged expressions ignore the transient behavior of the transfer numbers. In the present work, the Nu and Nu_{liq} numbers are expressed as a function of the non-dimensional time and this is an improvement of the model used in [61]; the correlations used are shown in Table 1 and they are valid for the conditions examined in the present work.

The results of the 0-D model by using the transient correlations for Nu and Nu_{liq} are shown in Fig. 10 for the case of $We = 45$ and three different gas phase temperatures; the solid and the dashed lines correspond to the CFD and the 0-D model predictions, respectively. As seen, the time dependent expressions for the transfer number can adequately predict the transient behavior of the surface temperature, with a less than 4 K error. The model predictions presented in Fig. 10 have assumed that the temporal evolution of the surface area is known and this is a limitation of the proposed model. On the other hand, Eqs. (8a)–(8c) for the surface area evolution can be used to predict the thermal behavior for $t < t_{sh}$; in this case, the errors are mainly determined by the effectiveness of the curve reproducing the surface area evolution.

In Strotos et al. [61] it was shown that droplet breakup is affected by heating when the We number is low and the ambient temperature is high. This conclusion was drawn both by considering the associated timescales (either in a macroscopic or a microscopic level) and by implementing the aforementioned 0-D model with the time-averaged expressions for the transfer numbers. These comments are also verified by the present simulations for an n-decane droplet. Relating the n-heptane CFD simulations performed in [61] and the present ones for the n-decane, the surface temperature at $t = t_{sh}$ is well represented by Eq. (16). This

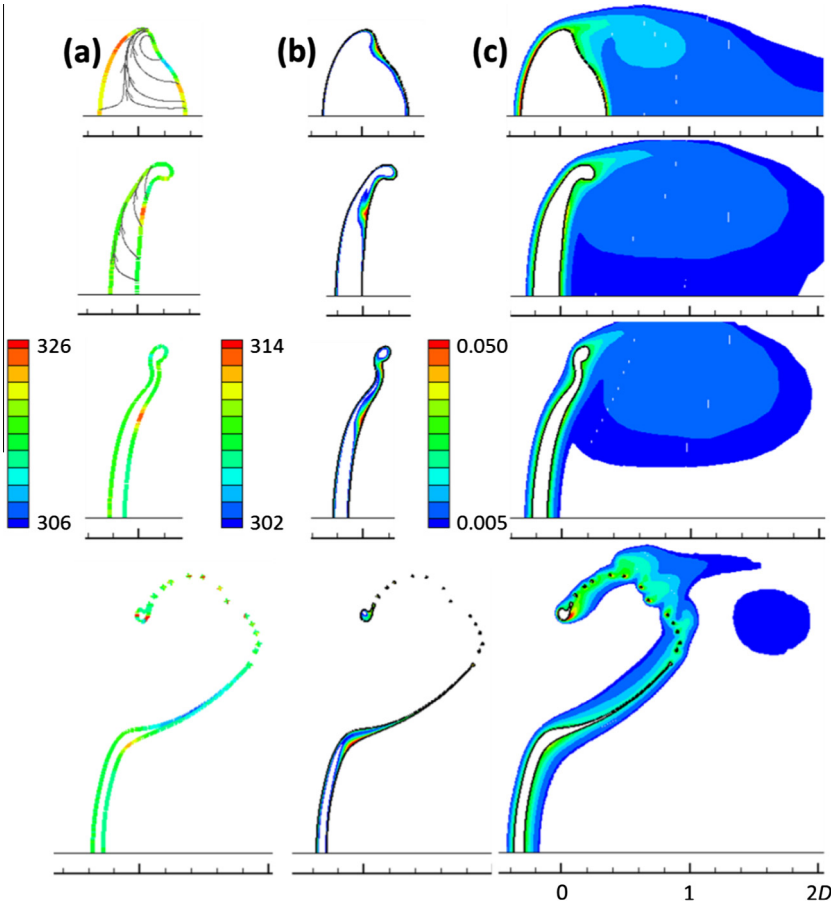

Fig. 12. Spatial distribution of (a) surface temperature, (b) droplet temperature and (c) vapor concentration for the case (We, T_∞) = (30, 800). The time instances presented are 0.5, 1.0, 1.25 and $1.5t_{sh}$. In (a) characteristic streamlines are also shown. For color interpretation, see the online version.

equation clearly demonstrates the effect of *We* number, gas phase temperature and species volatility through the heating factor F_{heat}:

$$T_s(t_{sh}) = T_0\left(1 + 0.0195We^{-0.2532}F_{heat}^{2.053}\right) \quad (16)$$

3.4. Spatial distribution of the flow variables

The spatial distribution of surface temperature, inner droplet temperature and vapor concentration field are shown in Figs. 11 and 12 for the cases with T_∞ = 800 K and *We* number 15 and 30, respectively. The surface temperature (denoted with a thick line colored with the corresponding temperature values) is not spatially uniform; along the droplet surface differences of 15 K can be observed. In the initial flattening phase, hot spots are observed on the front side of the droplet in an off-axis location; at subsequent instances hot spots are observed at the rear of the droplet. In a spherical droplet case these temperature differences along the surface could induce secondary flow (due to surface tension gradients) and form cellular vortices. The present work has included the effect of surface tension variation along the interface through the CSS surface tension model [76]. Nevertheless, no secondary flow was observed in the present cases (see characteristic streamlines in the left column), since the flow patterns are determined by the droplet shape. Regarding the inner temperature field and the vapor concentration field in the gas phase, these follow similar patterns to the ones observed in [61], as affected by the local velocity field and the droplet deformation.

4. Conclusions

The Navier-Stokes, energy and transport of species conservation equations together with the VOF methodology have been utilized to study the coupled problem of aerodynamic droplet breakup under the influence of heating and evaporation for *We* numbers in the range 15–90 and gas phase temperatures 600–1000 K. To quantify the effect of heating, the same cases were also studied under isothermal conditions assuming constant species properties. Combining the results obtained from the present work for an *n*-decane fuel droplet with those for a more volatile *n*-heptane droplet presented in Strotos et al. [61], it seems that droplet heating affects the overall breakup performance for low *We* numbers, high gas phase temperatures and low volatility fuels. For a non-breaking-up case with constant properties, heating may decrease the surface tension coefficient in such a way, that droplet not only breaks up in the bag breakup regime, but also in the transitional breakup regime. Nevertheless, at high *We* numbers the surface tension still decreases but without altering the breakup performance. During droplet breakup, despite the fact that the liquid evaporated mass is very low (especially for low volatility fuels), one has to consider the evaporation source terms since they play an important role by suppressing the droplet heat-up; this is evident for high volatility fuels which seem to be less affected by heating.

The concept of "heating factor" was introduced which provides an indication of the droplet tendency to heat-up by combining the terms tending to increase and decrease the droplet temperature. Useful correlations were provided for an a priori estimation of the breakup instant, surface area evolution and droplet heat-up. Additional to them, an enhanced 0-D model able to predict the thermal behavior of the droplet is proposed. In relevance to our previous work [61], it uses time-dependent transfer numbers instead of time-averaged and it is able to capture the transient behavior of the spatially average surface temperature. The latter is not spatially uniform and peak values are observed in the front of the droplet in the initial flattening phase and at the rear of the droplet in the subsequent stages.

Acknowledgements

The research leading to these results has received funding from the People Programme (Marie Curie Actions) of the European Union's Seventh Framework Programme FP7-PEOPLE-2012-IEF under REA grant Agreement No. 329116.

References

[1] Guildenbecher DR, López-Rivera C, Sojka PE. Secondary atomization. Exp Fluids 2009;46:371–402.
[2] Pilch M, Erdman C. Use of breakup time data and velocity history data to predict the maximum size of stable fragments for acceleration-induced breakup of a liquid drop. Int J Multiph Flow 1987;13:741–57.
[3] Faeth GM, Hsiang LP, Wu PK. Structure and breakup properties of sprays. Int J Multiph Flow 1995;21(Supplement):99–127.
[4] Gelfand BE. Droplet breakup phenomena in flows with velocity lag. Prog Energy Combust Sci 1996;22:201–65.
[5] Theofanous TG. Aerobreakup of newtonian and viscoelastic liquids. Annu Rev Fluid Mech 2011;43:661–90.
[6] Nicholls JA, Ranger AA. Aerodynamic shattering of liquid drops. AIAA J 1969;7:285–90.
[7] Krzeczkowski SA. Measurement of liquid droplet disintegration mechanisms. Int J Multiph Flow 1980;6:227–39.
[8] Hsiang LP, Faeth GM. Near-limit drop deformation and secondary breakup. Int J Multiph Flow 1992;18:635–52.
[9] Hsiang LP, Faeth GM. Drop properties after secondary breakup. Int J Multiph Flow 1993;19:721–35.
[10] Hsiang LP, Faeth GM. Drop deformation and breakup due to shock wave and steady disturbances. Int J Multiph Flow 1995;21:545–60.
[11] Chou WH, Hsiang LP, Faeth GM. Temporal properties of drop breakup in the shear breakup regime. Int J Multiph Flow 1997;23:651–69.
[12] Chou WH, Faeth GM. Temporal properties of secondary drop breakup in the bag breakup regime. Int J Multiph Flow 1998;24:889–912.
[13] Dai Z, Faeth GM. Temporal properties of secondary drop breakup in the multimode breakup regime. Int J Multiph Flow 2001;27:217–36.
[14] Liu Z, Reitz RD. An analysis of the distortion and breakup mechanisms of high speed liquid drops. Int J Multiph Flow 1997;23:631–50.
[15] Lee CH, Reitz RD. An experimental study of the effect of gas density on the distortion and breakup mechanism of drops in high speed gas stream. Int J Multiph Flow 2000;26:229–44.
[16] Cao X-K, Sun Z-G, Li W-F, Liu H-F, Yu Z-H. A new breakup regime of liquid drops identified in a continuous and uniform air jet flow. Phys Fluids 2007;19:057103.
[17] Zhao H, Liu H-F, Li W-F, Xu J-L. Morphological classification of low viscosity drop bag breakup in a continuous air jet stream. Phys Fluids 2010;22:114103.
[18] Zhao H, Liu H-F, Xu J-L, Li W-F, Lin K-F. Temporal properties of secondary drop breakup in the bag-stamen breakup regime. Phys Fluids 2013;25:054102.
[19] Opfer L, Roisman IV, Tropea C. Aerodynamic fragmentation of drops: dynamics of the liquid bag. In: ICLASS 2012, Heidelberg, Germany; 2012.
[20] Opfer L, Roisman IV, Venzmer J, Klostermann M, Tropea C. Droplet-air collision dynamics: evolution of the film thickness. Phys Rev E 2014;89:013023.
[21] Guildenbecher DR, Sojka PE. Experimental investigation of aerodynamic fragmentation of liquid drops modified by electrostatic surface charge. Atom Sprays 2011;21:139–47.
[22] Flock AK, Guildenbecher DR, Chen J, Sojka PE, Bauer HJ. Experimental statistics of droplet trajectory and air flow during aerodynamic fragmentation of liquid drops. Int J Multiph Flow 2012;47:37–49.
[23] Han J, Tryggvason G. Secondary breakup of axisymmetric liquid drops. II. Impulsive acceleration. Phys Fluids 2001;13:1554–65.
[24] Aalburg C. Deformation and breakup of round drop and nonturbulent liquid jets in uniform crossflows. In: Aerospace Engineering and Scientific Computing. University of Michigan; 2002.
[25] Khosla S, Smith CE. Detailed understanding of drop atomization by gas crossflow using the volume of fluid method. In: ILASS Americas, Toronto, Canada, 2006.
[26] Quan S, Schmidt DP. Direct numerical study of a liquid droplet impulsively accelerated by gaseous flow. Phys Fluids 2006;18:103103.
[27] Wadhwa AR, Magi V, Abraham J. Transient deformation and drag of decelerating drops in axisymmetric flows. Phys Fluids 2007;19:113301.
[28] Xiao F, Dianat M, McGuirk JJ. LES of single droplet and liquid jet primary breakup using a coupled level set/volume of fluid method. In: 12th ICLASS, Heidelberg, Germany, 2012.
[29] Khare P, Yang V. Drag coefficients of deforming and fragmenting liquid droplets. In: ILASS Americas, 2013.
[30] Jalaal M, Mehravaran K. Transient growth of droplet instabilities in a stream. Phys Fluids 2014;26:012101.
[31] Jain M, Prakash RS, Tomar G, Ravikrishna RV. Secondary breakup of a drop at moderate Weber numbers. Proceed Roy Soc Lond A: Math, Phys Eng Sci 2015;471.
[32] Yang W, Jia M, Sun K, Wang T. Influence of density ratio on the secondary atomization of liquid droplets under highly unstable conditions. Fuel 2016;174:25–35.

[33] Strotos G, Malgarinos I, Nikolopoulos N, Gavaises M. Predicting droplet deformation and breakup for moderate Weber numbers. Int J Multiph Flow 2016;85:96–109.
[34] Givler SD, Abraham J. Supercritical droplet vaporization and combustion studies. Prog Energy Combust Sci 1996;22:1–28.
[35] Bellan J. Supercritical (and subcritical) fluid behavior and modeling: drops, streams, shear and mixing layers, jets and sprays. Prog Energy Combust Sci 2000;26:329–66.
[36] Sazhin SS. Advanced models of fuel droplet heating and evaporation. Prog Energy Combust Sci 2006;32:162–214.
[37] Erbil HY. Evaporation of pure liquid sessile and spherical suspended drops: a review. Adv Colloid Interface Sci 2012;170:67–86.
[38] Renksizbulut M, Haywood RJ. Transient droplet evaporation with variable properties and internal circulation at intermediate Reynolds numbers. Int J Multiph Flow 1988;14:189–202.
[39] Haywood RJ, Nafziger R, Renksizbulut M. Detailed examination of gas and liquid phase transient processes in convective droplet evaporation. J Heat Transfer 1989;111:495–502.
[40] Chiang CH, Raju MS, Sirignano WA. Numerical analysis of convecting, vaporizing fuel droplet with variable properties. Int J Heat Mass Transf 1992;35:1307–24.
[41] Megaridis CM. Comparison between experimental measurements and numerical predictions of internal temperature distributions of a droplet vaporizing under high-temperature convective conditions. Combust Flame 1993;93:287–302.
[42] Shih AT, Megaridis CM. Suspended droplet evaporation modeling in a laminar convective environment. Combust Flame 1995;102:256–70.
[43] Shih AT, Megaridis CM. Thermocapillary flow effects on convective droplet evaporation. Int J Heat Mass Transf 1996;39:247–57.
[44] Abou Al-Sood MM, Birouk M. A numerical study of the effect of turbulence on mass transfer from a single fuel droplet evaporating in a hot convective flow. Int J Therm Sci 2007;46:779–89.
[45] Raghuram S, Raghavan V, Pope DN, Gogos G. Two-phase modeling of evaporation characteristics of blended methanol–ethanol droplets. Int J Multiph Flow 2013;52:46–59.
[46] Schlottke J, Weigand B. Direct numerical simulation of evaporating droplets. J Comput Phys 2008;227:5215–37.
[47] Ghata N, Shaw BD. Computational modeling of the effects of support fibers on evaporation of fiber-supported droplets in reduced gravity. Int J Heat Mass Transf 2014;77:22–36.
[48] Megaridis CM, Sirignano WA. Numerical modeling of a vaporizing multicomponent droplet. Symp (Int) Combust 1990;23:1413–21.
[49] Megaridis CM, Sirignano WA. Multicomponent droplet vaporization in a laminar convective environment. Combust Sci Technol 1992;87:27–44.
[50] Megaridis CM. Liquid-phase variable property effects in multicomponent droplet convective evaporation. Combust Sci Technol 1993;92:291–311.
[51] Renksizbulut M, Bussmann M. Multicomponent droplet evaporation at intermediate Reynolds numbers. Int J Heat Mass Transf 1993;36:2827–35.
[52] Strotos G, Gavaises M, Theodorakakos A, Bergeles G. Numerical investigation of the evaporation of two-component droplets. Fuel 2011;90:1492–507.
[53] Banerjee R. Numerical investigation of evaporation of a single ethanol/iso-octane droplet. Fuel 2013;107:724–39.
[54] Strotos G, Malgarinos I, Nikolopoulos N, Gavaises M. Predicting the evaporation rate of stationary droplets with the VOF methodology for a wide range of ambient temperature conditions. Int J Therm Sci 2016;109:253–62.
[55] Haywood RJ, Renksizbulut M, Raithby GD. Numerical solution of deforming evaporating droplets at intermediate Reynolds numbers. Numer Heat Transf; A: Appl 1994;26:253–72.
[56] Haywood RJ, Renksizbulut M, Raithby GD. Transient deformation and evaporation of droplets at intermediate Reynolds numbers. Int J Heat Mass Transf 1994;37:1401–9.
[57] Mao ZS, Li T, Chen J. Numerical simulation of steady and transient mass transfer to a single drop dominated by external resistance. Int J Heat Mass Transf 2001;44:1235–47.
[58] Hase M, Weigand B. Transient heat transfer of deforming droplets at high Reynolds numbers. Int J Numer Meth Heat Fluid Flow 2003;14:85–97.
[59] Schlottke J, Dulger E, Weigand B. A VOF-based 3D numerical investigation of evaporating, deformed droplets. Progr Comput Fluid Dyn, Int J 2009;9:426–35.
[60] Cerqueira RFL, Paladino EE, Maliska CR. A computational study of the interfacial heat or mass transfer in spherical and deformed fluid particles flowing at moderate Re numbers. Chem Eng Sci 2015;138:741–59.
[61] Strotos G, Malgarinos I, Nikolopoulos N, Gavaises M. Numerical investigation of aerodynamic droplet breakup in a high temperature gas environment. Fuel 2016;181:450–62.
[62] Theodorakakos A, Bergeles G. Simulation of sharp gas–liquid interface using VOF method and adaptive grid local refinement around the interface. Int J Numer Meth Fluids 2004;45:421–39.
[63] Malgarinos I, Nikolopoulos N, Marengo M, Antonini C, Gavaises M. VOF simulations of the contact angle dynamics during the drop spreading: standard models and a new wetting force model. Adv Colloid Interface Sci 2014;212:1–20.
[64] Perry RH, Green DW. Perry's chemical engineers' handbook. 7th ed. McGraw-Hill; 1997.
[65] Poling BE, Prausnitz JM, O'Connell JP. Properties of Gases and Liquids. 5th ed. McGraw-Hill; 2001.
[66] ANSYS®FLUENT, Release 14.5, Theory Guide; 2012.
[67] Malgarinos I, Nikolopoulos N, Gavaises M. Coupling a local adaptive grid refinement technique with an interface sharpening scheme for the simulation of two-phase flow and free-surface flows using VOF methodology. J Comput Phys 2015;300:732–53.
[68] Strotos G, Malgarinos I, Nikolopoulos N, Papadopoulos K, Theodorakakos A, Gavaises M. Performance of VOF methodology in predicting the deformation and breakup of impulsively accelerated droplets. In: 13th ICLASS, Tainan, Taiwan, 2015.
[69] Clift R, Grace JR, Weber ME. Bubbles, drops and particles. New York: Academic Press; 1978.
[70] Michaelides EE. Particles, bubbles & drops: their motion, heat and mass transfer. World Scientific; 2006.
[71] Incropera FP, de Witt DP. Fundamentals of heat and mass transfer. 3rd ed. New York: Wiley; 1990.
[72] Seki M, Kawamura H, Sanokawa K. Transient temperature profile of a hot wall due to an impinging liquid droplet. J Heat Transfer 1978;100:167–9.
[73] Strotos G, Aleksis G, Gavaises M, Nikas K-S, Nikolopoulos N, Theodorakakos A. Non-dimensionalisation parameters for predicting the cooling effectiveness of droplets impinging on moderate temperature solid surfaces. Int J Therm Sci 2011;50:698–711.
[74] Strotos G, Nikolopoulos N, Nikas K-S, Moustris K. Cooling effectiveness of droplets at low Weber numbers: effect of temperature. Int J Therm Sci 2013;72:60–72.
[75] Renksizbulut M, Bussmann M, Li X. Droplet vaporization model for spray calculations. Part Part Syst Charact 1992;9:59–65.
[76] Lafaurie B, Nardone C, Scardovelli R, Zaleski S, Zanetti G. Modelling merging and fragmentation in multiphase flows with SURFER. J Comput Phys 1994;113:134–47.